Global stability and optimal perturbation for a jet in cross-flow

CrossMark

A. Peplinski, P. Schlatter *, D.S. Henningson

Linné FLOW Centre and Swedish e-Science Research Centre (SeRC), KTH Mechanics, Royal Institute of Technology, SE-100 44 Stockholm, Sweden

A R T I C L E   I N F O

A B S T R A C T

We study the stability of a jet in cross-flow at low values of the jet to cross-flow velocity ratio R using direct numerical simulations (DNS) and global linear stability analysis adopting a time-stepper method. For the simplified setup without a meshed pipe in the simulations we compare results of a fully-spectral code SIMSON with a spectral-element code Nek5000. We find the use of periodic domains, even with the fringe method, unsuitable due to the large sensitivity of the eigenvalues and due to the large spatial growth of the corresponding eigenmodes. However, we observe a similar sensitivity to reflection from the outflow boundary in the inflow/outflow configuration, and therefore we use an extended domain where reflections are minimal. We apply in our studies both modal and non-modal linear analyses investigating transient effects and their asymptotic fate, and we find a transient wavepacket to develop almost identically in both the globally stable and unstable cases. The final results of the global stability analysis for our numerical setup show the critical value of R, at which the first bifurcation occurs, to lie in the range between 1.5 and 1.6.

© 2014 Elsevier Masson SAS. All rights reserved.

1. Introduction

The so-called jet in cross-flow (JCF) refers to fluid that exits a nozzle and interacts with the surrounding boundary layer flowing across the nozzle. This case has been extensively studied both experimentally [1–6], theoretically [7,8] and numerically [9–15] over the past decades due to its high practical relevance. Smoke and pollutant plumes, fuel injection and mixing or film cooling are just a few applications. On the other hand, the jet in cross-flow is considered a canonical flow problem featuring complex, fully three-dimensional dynamics that cannot be investigated under simplifying assumptions commonly applied to simpler flows. It makes the JCF a perfect tool for testing numerical methods for studying the stability of fluid flows and simulation capabilities. Recent reviews on this flow configuration are given in Refs. [16,17].

In this work we concentrate on the incompressible flow with the round perpendicular jet of constant diameter and characterise the JCF by three independent non-dimensional parameters: the free-stream and jet Reynolds numbers ($Re_{\delta_0^\star}$, Re_{jet}) and jet to free-stream velocity ratio R, which is the key parameter here. The major flow features are (see Fig. 1): the counter-rotating vortex pair (CVP) in the far field, the horseshoe vortex placed upstream of the jet orifice [18], and vortices shed from the shear layers

caused by the interaction of the jet with the cross-flow. There are other features observed at higher values of the cross velocity ratio R, e.g., wake vortices [1] and upright vortices [14]. As the ratio R increases, the flow evolves from a stable (and thus steady) configuration consisting of a (steady) CVP and horseshoe vortex (Fig. 2), through simple periodic shear layer vortex shedding (a limit cycle; Fig. 16) to more complicated quasi-periodic behaviour, before finally becoming turbulent. The breakup of the CVP due to interaction with vortices shed from the shear layer is also illustrated in Fig. 2 in Ref. [15].

Laminar–turbulent flow transition is a classical problem in fluid mechanics. Initially motivated by aerodynamic applications, it is an important phenomenon in many other industrial applications. Originally, hydrodynamic stability was studied by means of linear stability theory investigating the behaviour of infinitesimal disturbances in space and time around some basic flow state. In the so-called local analysis, the exponential growth of linear perturbations is studied at each streamwise position and the distinction between local convective and absolute stability is made [19]. This local treatment is legitimate for parallel and weakly non-parallel flows, but many of the flow configurations developing strong instabilities and eventually exhibiting transition to turbulence (e.g. JCF) are strongly non-parallel. Moreover, they belong to the open flow category, where fluid particles continuously enter and leave the considered domain. Such unstable open flows require global analysis where the evolution of perturbations is considered in the whole physical domain [20]. The

* Corresponding author. Tel.: +46 8 790 71 76.
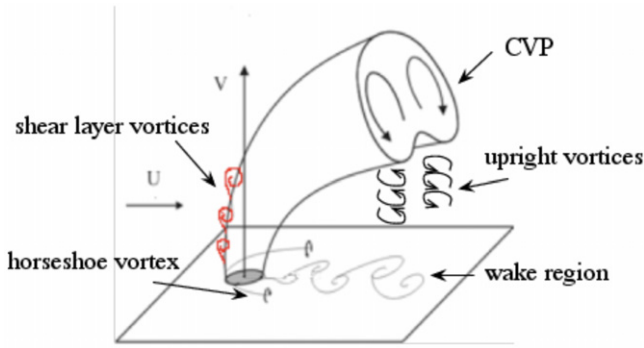*E-mail address:* pschlatt@mech.kth.se (P. Schlatter).

Fig. 1. A sketch of the main vortical structures that may be identified in the jet in cross-flow.
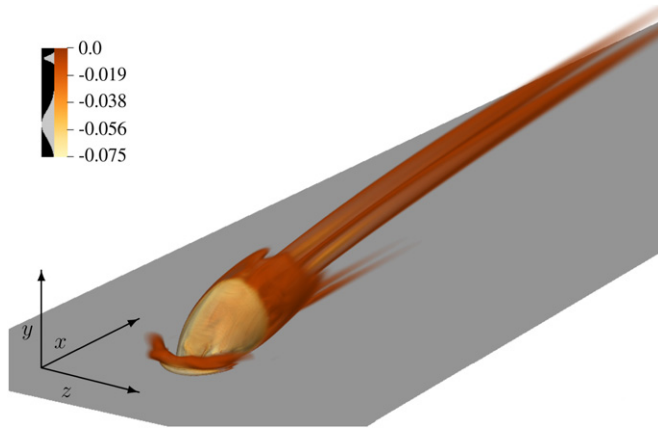*Source:* Figure adopted from Ref. [15].

Fig. 2. Vortical structure of the base flow $\vec{U}_b$ for the JCF with $R = 1.5$ obtained with SFD for mesh MS3 and $N = 9$. The steady CVP, shear layer and horse shoe vortex are clearly visible. The vortical structure is presented using volume rendering of the λ_2 vortex identification criterion [39]. Highly negative values of λ_2 are coloured in yellow (vortex 'cores'), and the regions of lower magnitude, i.e., negative value closer to zero, are coloured in brown (vortex 'edges'). (For interpretation of the references to colour in this figure legend, the reader is referred to the web version of this article.)

global behaviour of the flow depends on the competition between local instability and basic advection. The linear global modes are the eigenmodes of the linearised Navier–Stokes operator. The recent review of the work on global stability in the past years can be found, e.g., in Theofilis [21].

The first linear global stability analysis of the JCF in a simplified setup not including the pipe in the computational domain at $R = 3$ was presented by Bagheri et al. [13,14]. In this work the pipe orifice was represented by the Dirichlet boundary conditions. For this jet to free-stream velocity ratio the JCF was found to be dominated by an interplay of three common instability mechanisms: a Kelvin–Helmholtz shear layer instability, a possible elliptic instability of the CVP, and a near-wall vortex shedding mechanism similar to a von Kármán vortex street. It was also shown that the flow acts as an oscillator, with high-frequency unstable global eigenmodes associated with shear-layer instabilities on the CVP and low-frequency modes resulting in vortex shedding in the jet wake. This work was later extended to the wider range of $R \in (0.55, 2.75)$ by Ilak et al. [15], focusing on transition from steady to unsteady flow as R is increased. The first bifurcation i.e., the appearance of the first unstable eigenmode, was found to occur at $R \approx 0.675$, when shedding of hairpin vortices characteristic of a shear layer instability was observed, and the source of this instability (*wavemaker*) was located in the shear layer just downstream of the orifice. Results of linear stability analysis were consistent with nonlinear direct numerical simulations (DNS) at the

critical value of R predicting well the frequency and initial growth rate of the disturbance. It was also concluded that, based on linear analysis, good qualitative predictions about the flow dynamics can be made even for higher values of R, where multiple unstable eigenmodes are present. The authors pointed out, however, that the critical value of R cannot be determined exactly due to sensitivity of the results to changes in the domain length as well as to the presence of the fringe region enforcing periodic boundary condition (BC).

In the current study we follow Ilak et al. [15] focusing on the transition from steady to unsteady flow and, using linear global stability analysis, searching for the value of R at which the first bifurcation occurs. The scope of this work is to study global stability of the JCF focusing on the eigenmode sensitivity to the simulation parameters. This way we test the numerical methods and identify the major practical difficulties related to linear stability of this type of complex flows.

However, as purely modal analysis is known to fail in predicting the practically observed critical Reynolds number for transition to turbulence in a number of systems [22–29], we apply in our studies both modal and non-modal analyses. A classical example of such a flow is the convectively unstable flat-plate boundary layer [30], which behaves as broadband amplifier for incoming disturbances, but is globally stable according to linear global analysis. However, a global stability analysis based on the asymptotic behaviour of single eigenmodes of the system does not capture all relevant dynamics, and transition to turbulence at finite Re occurs due to transient effects. Following Ref. [31] we investigate the linear growth of perturbations in the JCF for a limited time, before the exponential modal behaviour is most dominant, and determine an *optimal initial condition* (initial condition yielding largest possible growth in energy) adopting a time-stepper method.

This paper is organised as follows. Section 2 describes the numerical methods used for modal and non-modal stability calculations including a brief description of the employed codes. In this section we also give details of computational setup. Section 3 is devoted to the global stability of the JCF. We discuss here results obtained by DNS and linear modal analysis focusing on the sensitivity of bifurcation point to various simulation parameters and employed code. Results of non-modal analysis are presented in Section 4 and the final discussion with conclusions is given in Section 5.

2. Simulation setup and numerical method

We adopt the same computational setup as Ilak et al. [15], modelling the interaction of a boundary layer with a perpendicular jet exiting a circular pipe with diameter $D = 3\delta_0^\star$, where $\delta_0^\star$ is the displacement thickness at the inflow placed $9.375 \cdot \delta_0^\star$ upstream of the centre of the pipe orifice. In our calculations $\delta_o^\star$ is used as reference length unit. Following Ref. [15] we use both a laminar cross-flow and jet inflow profile and, as the jet pipe is absent in our simulations, an inhomogeneous (Dirichlet) BC prescribing the inflow jet profile is employed instead. This is an important limitation of the problem setup requiring, e.g., smoothing of the jet profile by a super-exponential Gaussian function;

$$v(r) = V(1 - r^2) \exp(-(r/0.7)^4),$$

where v is the wall-normal velocity, V is the *peak* jet velocity, and r is the distance from the centre of the jet nozzle (x_{jet}, z_{jet}), defined as:

$$r = (2/D)\sqrt{(x - x_{jet})^2 + (z - z_{jet})^2}.$$

A full discussion on this choice of profile can be found in Refs. [13,15].

Table 1

Mesh parameters for different simulation setups. Simulations performed with SIMSON use mesh MS1 with uniform resolution in x and z directions. Meshes MS2–MS4 have nonuniform resolution dependent on polynomial order N and are used in Nek5000 simulations. In this case the total number of elements (dependent on L_x), mesh type (resolution in the wall vicinity) and polynomial order are given. Both mesh types R1 and R2 keep highest (uniform) resolution in the vicinity of the jet inflow, however, in R2 a single, unit height layer of elements next to the wall is replaced by two layers of elements. This way the vertical resolution in the wall vicinity is doubled. Each element consists of $N + 1 \times N + 1 \times N + 1$ Gauss–Lobatto–Legendre points.

Mesh	L_x	L_y	L_z	Mesh structure	N
MS1	150	20	30	$512 \times 201 \times 144$	
MS2	150	20	30	R1; 37440 elements	6, 9
MS3	150	20	30	R2; 39520 elements	6, 9
MS4	250	30	30	R1; 68640 elements	9, 12

The flow is fully described by the dimensionless (in units of $\delta_0^\star$) pipe diameter D, cross-flow Reynolds number $Re_{\delta_0^\star} = U_\infty \delta_0^\star / \nu$ and jet to cross-flow velocity ratio $R = V/U_\infty$, where U_∞ and ν are free-stream velocity and the kinematic viscosity, respectively. We have to mention here that there are a number of possible definitions of the jet to cross-flow velocity ratio, based e.g. on the mass flux, however, to be able to compare our results with Ilak et al. [15] we follow in this work Ref. [13] using the peak jet inflow velocity V to calculate R. The jet Reynolds number based on the jet velocity and the jet diameter $Re_{jet} = VD/\nu$ is in our case a function of the velocity ratio and cross-flow Reynolds number $Re_{jet} = Re_{\delta_0^\star} RD/\delta_o^\star$. To be consistent with Ilak et al. [15] we set $U_\infty = 1$, $Re_{\delta_0^\star} = 165$, and choose R as 1.0, 1.4, 1.5 and 1.6. We list here only the key parameters of the setup and refer the reader to Refs. [13,15] for more details.

The size of the computational domain and adopted resolutions depend on the employed code and studied case. They are discussed in the following sections, and the key mesh parameters used for all simulations are summarised in Table 1.

2.1. Direct numerical simulations

As the adopted numerical method for both modal and non-modal analyses is based on the time-stepper method, where the matrix action on a vector is given by the linear DNS iterations, we start our discussion from a short description of the employed DNS codes. Both linear and nonlinear simulations are performed with two different massively parallel DNS solvers for the incompressible Navier–Stokes equations: SIMSON [32] and Nek5000 [33].

SIMSON was used in Refs. [13–15] for the JCF and is a fully-spectral code well suited for stability computations. In this code the wall-parallel directions are discretised using Fourier series and the wall-normal direction using Chebyshev series. A major constraint is the requirement for periodic BC in the streamwise direction necessitating a fringe region for damping disturbances. The forcing $\vec{f}$ in the fringe region [34] has the form

$$\vec{f} = \lambda(x)(\vec{U}_F - \vec{u}), \tag{1}$$

where $\lambda(x)$ is a smooth step function, $\vec{U}_F$ is the desired flow solution in the fringe region (Blasius boundary layer in the studied case) and $\vec{u}$ is the current velocity field. This damping in the fringe region depends on the fringe length L_F and its strength, which is related to the shape of the step function $\lambda(x)$ (see Ch. 4.2.2 in Ref. [32]). We use SIMSON to investigate the influence of L_F on the stability results in nonlinear DNS while keeping the forcing strength constant. The fringe parameters are adopted from Ilak et al. [15] with varying L_F set to 15 (like in [15]), 45 and 75 in $\delta_0^\star$ units. As the fringe region reduces the useful part of the computational domain, we doubled the length of the box as compared to Ref. [15] setting its size to $L_x = 150$, $L_y = 20$, $L_z = 30$,

with the resolution of $512 \times 201 \times 144$ spectral collocation points in the streamwise (x), wall-normal (y), and spanwise (z) directions, respectively (mesh MS1).

Nek5000 is a spectral-element code locally providing spectral accuracy while allowing for complex geometries, however in current work we limit ourselves to simple setup considered in Ref. [15]. In the spectral element method (SEM) the governing equations are cast into weak form and discretised in space by the Galerkin approximation, following the $P_N - P_{N-2}$ approach with the velocity space spanned by Nth-order Lagrange polynomial interpolants. In our studies we use Nek5000 to investigate the influence of resolution (polynomial order $N = 6$, 9 and 12), box length ($L_x = 150$ and 250) and grid structure. Domain decomposition into hexahedral elements is used to reduce resolution where it is not needed. We keep the uniform resolution in the jet vicinity within 5 $\delta_0^\star$ units from the orifice, and reduce it at larger distance by smooth element stretching (resolution R1). In resolution R2 we double the vertical resolution close to the wall. There are no periodic BCs in the streamwise direction. We found our results to be dependent, however, on the outflow BC unless we set a sponge layer at the outflow in addition to making the computational domain longer to reduce reflections from the boundary. The forcing function for the sponge was adopted from the fringe in SIMSON (Eq. (1)), and the sponge length L_S was set to 25 and 35 units for $L_x = 150$ and 250, respectively. Nek5000 was also used as time-stepper for solving the linearised Navier–Stokes equations in modal and non-modal linear stability analyses. In the case of modal linear stability analysis and $L_x = 250$ we increase the height of the computational domain to $L_y = 30$ to ensure the CVP fit within the box. The mesh parameters are summarised in Table 1. It gives the mesh dimensions (L_x, L_y, L_z), vertical mesh resolution next to the wall (R1 versus R2 resolution), total element number (dependent on L_x) and adopted polynomial order N.

More detailed descriptions of the implementation of Nek5000 can be found in Fischer et al. [33].

2.2. Modal analysis

Modal stability analysis is the classical method of linear hydrodynamics stability investigating exponentially growing or decaying disturbances. It allows to compute the critical value of a given parameter, for which a single exponentially growing disturbance exists. In the linear theory for global analysis those disturbances, the so-called linear global modes, are associated with eigenmodes of the linearised Navier–Stokes operator (LNS) [35]. It allows to determine several characteristics: the parameters (e.g. R) at which the flow first becomes unstable, and the frequencies ω_r, growth rates ω_i and spatial structure of the linear perturbations (eigenmodes).

We consider the incompressible Navier–Stokes equations linearised about a base flow $\vec{U}_b$ in non-dimensional form with $\vec{u}$, p and $Re_{\delta_0^\star}$ being velocity and pressure perturbations and the Reynolds number, respectively,

$$\frac{\partial \vec{u}}{\partial t} + \vec{u} \cdot \nabla \vec{U}_b$$
$$+ \vec{U}_b \cdot \nabla \vec{u}$$
$$- \frac{1}{Re_{\delta_0^\star}} \nabla^2 \vec{u} + \nabla p = \vec{f} \quad \text{in } \Omega, \tag{2}$$

$$\nabla \cdot \vec{u} = 0 \quad \text{in } \Omega, \tag{3}$$

$$\vec{u} = 0 \quad \text{on } \partial\Omega_v, \tag{4}$$

$$p\vec{n} - \frac{1}{Re_{\delta_0^\star}} \nabla \vec{u} \cdot \vec{n} = 0 \quad \text{on } \partial\Omega_o. \tag{5}$$

The two last equations are the boundary conditions (BCs) on the surface of the computational domain Ω. Subscripts v and o stand for regions where either *velocity* (Dirichlet) or *outflow* BCs are specified, and $\vec{n}$ denotes the outward normal. The forcing $\vec{f}$ usually vanishes inside Ω, but may be used for sponge/fringe layers at inflow/outflow boundary as given by Eq. (1). In our calculations we replace outflow BC (Eq. (5)) with *velocity* BC $\vec{u} = 0$ applied on $\partial\Omega_o$. It is necessary to keep direct and adjoint LNS consistent in the non-modal analysis (Section 2.3). Note that this choice of BCs can change significantly the growth rates of the weaker modes leaving however unchanged the strongest ones. The dependency of the operator spectra on the applied BC for the flow past circular cylinder case is discussed in Peplinski et al. [36].

The eigenvalue problem is then constructed rewriting the LNS equations in operator form

$$\dot{\vec{u}} = \mathbf{A}\vec{u},$$

and assuming

$$\vec{u}(\vec{x}, t) = \hat{\vec{u}}(\vec{x}) \exp(-i\omega t),$$

where $\hat{\vec{u}}(\vec{x})$ is the global mode and $\omega = \omega_r + i\omega_i$ its complex eigenvalue. For general 3D flows, the size of the matrix $\mathbf{A}$ prohibits its explicit construction, so we adopt special matrix-free methods based on time-steppers [37,13], where the action of $\mathbf{A}$ on the vector $\vec{u}$ can be calculated. This method is an iterative technique based on orthogonal projection of $\mathbf{A}$ onto a lower-dimensional Krylov subspace, in which the Arnoldi algorithm is applied and the Krylov subspace is constructed using snapshots taken from the evolution of the flow field $\vec{u}$. In our implementation we use the implicitly restarted Arnoldi method (IRAM) from the ARPACK library [38]. We solve for the generalised eigenvalue problem

$$\mathbf{A}\hat{\vec{u}} = -i\omega \mathbf{B}\hat{\vec{u}},$$

where $\mathbf{B}$ is the mass matrix. It allows us to simplify the treatment of the duplicated values of the velocity field at the element faces, and to get the exact value of the inner product using correct weights applied in the orthogonalisation step.

To obtain the base flow $\vec{U}_b$ (Fig. 2) one has to find the steady state solution of the nonlinear Navier–Stokes equations, which in many of the considered cases is unstable, in particular for strongly convectively unstable flows (*e.g.* JCF). We compute the base flow using selective frequency damping (SFD) [40], which damps the oscillations of the unsteady part of the solution using a temporal low-pass filter by setting the forcing

$$\vec{f} = -\chi(\vec{u} - \vec{w})$$

in the whole computational domain Ω, where $\vec{u}$ is the flow solution and $\vec{w}$ its temporally low-pass-filtered counterpart obtained by a differential exponential filter

$$\dot{\vec{w}} = (\vec{u} - \vec{w})/\Delta.$$

In our simulations we set $\chi = 0.6$ and $\Delta = 1.91$. A good indicator of convergence is the amplitude of the forcing $\epsilon = \|(\vec{u} - \vec{w})\|/\Omega_{volume}$, which in all modelled cases reached 10^{-10}. It is considerably lower than the tolerance used for eigenvalue calculation (10^{-6}).

Detailed description of the implementation in Nek5000 and validation on the number of flow cases can be found in Peplinski et al. [36].

2.3. Non-modal analysis

The study of linear optimal disturbances is a well established technique to identify the initial condition leading to the largest growth of the disturbance at finite time. We look for the perturbation $\vec{u}(t = 0)$ which leads to maximum energy $\langle \vec{u}(T), \vec{u}(T) \rangle$ at time T, with $\langle \cdot, \cdot \rangle$ being the inner product. This problem is equivalent to solving the eigenvalue problem

$$\lambda \vec{u}(0) = \exp(\mathbf{A}^\dagger T) \exp(\mathbf{A}T) \vec{u}(0), \tag{6}$$

where $\exp(\mathbf{A}^\dagger T) \exp(\mathbf{A}T)$ is the composite of the forward and adjoint propagators, and $\mathbf{A}$ is the linearised Navier–Stokes operator. Its adjoint $\mathbf{A}^\dagger$ operator is defined by the property $\langle \vec{u}^\dagger, \mathbf{A}\vec{u} \rangle = \langle \mathbf{A}^\dagger \vec{u}^\dagger, \vec{u} \rangle$ and is written as

$$\frac{\partial \vec{u}^\dagger}{\partial t} + (\nabla \vec{U}_b)^T \vec{u}^\dagger$$

$$-\vec{U}_b \cdot \nabla \vec{u}^\dagger$$

$$+ \frac{1}{Re_{\delta_0^\star}} \nabla^2 \vec{u}^\dagger + \nabla p^\dagger = \vec{f} \quad \text{in } \Omega, \tag{7}$$

$$\nabla \cdot \vec{u}^\dagger = 0 \quad \text{in } \Omega, \tag{8}$$

$$\vec{u}^\dagger = 0 \quad \text{on } \partial\Omega_v, \tag{9}$$

$$p^\dagger \vec{n} + \frac{1}{Re_{\delta_0^\star}} \nabla \vec{u}^\dagger \cdot \vec{n} = (\vec{U}_b \cdot \vec{n}) \vec{u}^\dagger \quad \text{on } \partial\Omega_o, \tag{10}$$

where $\vec{u}^\dagger$ and $p^\dagger$ are adjoint perturbations. Notice the change of sign in the equations and the fact that *outflow* BCs are inhomogeneous. However, Nek5000 does not support general inhomogeneous BC as given above. Therefore, to keep direct and adjoint problems consistent we set homogeneous Dirichlet BC on all $\partial\Omega$. To avoid reflections we use a sponge layer at the inflow and outflow boundaries.

The largest eigenvalue can be found iteratively by (matrix-free) power iterations of Eq. (6), where the state is first marched forward in time with the standard numerical solver (direct propagator) and then backward with the corresponding adjoint solver (adjoint propagator). The initial condition is white noise and the procedure is repeated until the assumed convergence criterion for $\|\vec{u}_n(0) - \vec{u}_{n-1}(0)\|$ is reached, where n is the iteration number and both $\vec{u}_n(0)$ and $\vec{u}_{n-1}(0)$ are rescaled to the same energy level. For a more detailed discussion and description of implementation in Nek5000 see Ref. [41].

3. Global stability

To investigate the global stability of the JCF and the dependence of the critical inflow ratio R value on the various simulation parameters we performed a number of nonlinear DNS using SIMSON and Nek5000, and linear global stability analysis with Nek5000. Results are discussed in the following sections.

3.1. Nonlinear direct numerical simulations

The study results pertaining to the sensitivity to damping in the fringe for $R = 1$ were performed with SIMSON and are presented in Fig. 3. The figure shows the energy of a single, most dominant Fourier component of the streamwise velocity component integrated over y–z plane and plotted as a function of streamwise position x. It was calculated by performing the Fourier transform in time at every spatial position (x, y, z) on eight snapshots of the velocity field saved within a local temporal window ($t - T_p/2$, $t + T_p/2$). T_p is here the period of the oscillations found in the signal of the streamwise velocity component of a probe located 15 units downstream of the pipe centre. Continuous, dashed and dotted curves give the energy distribution at time $t = 500$ and correspond to different fringe lengths L_F equal to 15, 45 and 75 units, respectively. Time is counted from the beginning of simulation and
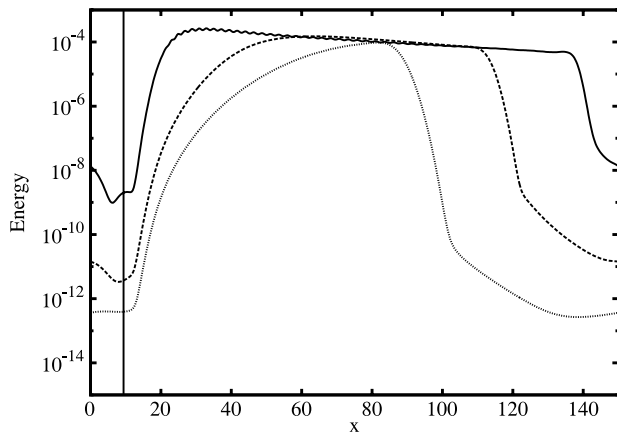
Fig. 3. Energy as a function of streamwise position of the single dominant Fourier component for $R = 1$ and different fringe lengths L_F equal to 15 (continuous line), 45 (dashed line) and 75 (dotted line) units. Simulation results of SIMSON obtained on mesh MS1.

Fig. 4. Growth rate of the strongest mode as the function of polynomial order N for different mesh structures. Symbols $+$ and $\times$ present results of the modal stability analysis for $R = 1.5$ and meshes MS2 and MS3 respectively. Symbols $\triangle$ and $\bigcirc$ show results of modal stability analysis for $R = 1.6$ and meshes MS3 and MS4. Simulations using Nek5000.

the jet centre is marked by the vertical line. The first simulation was performed with $L_F = 15$ and Blasius boundary layer as initial condition, and run up to $t = 880$, when the probe signal saturated. This state provided the initial conditions for the two other runs. There are three main regions located downstream to the pipe orifice, corresponding to exponential spatial growth, nonlinear saturation and damping in the fringe region. The length of the fringe layer is clearly visible. For L_F equal to 15 and 45 units the signal saturates reaching an approximate steady state, and only for the longest fringe the energy maximum decreases continuously with time. This shows the JCF at $R = 1$ to be a globally stable noise amplifier.

According to Ilak et al. [15] the JCF for $R = 1$ appears globally unstable, however, closer examination of our results shows this flow to be in fact convectively unstable, and the misinterpretation of the instability mechanism stems from insufficient damping in the fringe. The temporal amplitude evolution of the simulation with the shortest fringe features a short phase of approximately exponential decay (after an initial transient phase). This phase ends when the signal from the fringe reaches the jet orifice after re-entering the domain, and triggers an instability. It is because the damping in the fringe region (of the order of 10^5) is too weak compared to the growth rate in the domain leading to nonlinear saturation of the signal. Similar conclusions can be drawn from the second run ($L_F = 45$; Fig. 3), where the nonlinear saturation on the energy plot is still visible. To achieve sufficient damping a fringe with at least $L_F = 75$ (50% of the computation domain) is required. In this case the signal amplitude decays exponentially and the saturation is no longer visible after 500 time units. However, even in this case the decay rate after $t = 400$ is relatively low leaving a considerable amount of energy in the strongest Fourier mode after $t = 1500$. This shows that simulation methods relying on periodic domains to be unsuited for flow cases with considerable spatial growth rates unless extreme care is taken to ensure sufficient damping in the fringe region. To employ such methods one has to ensure the fringe damping is larger than the expected (physical) spatial growth in the domain to make perturbations re-entering the domain not relevant for the flow dynamics (see as well Ref. [42]).

Due to these problems with the periodic setup all subsequent runs are performed with Nek5000, which allows inflow/outflow BC in streamwise direction. Nevertheless, even in this case a careful treatment of outflow BC was found to be crucial. In the presented simulations, the *outflow* BC Eq. (5) together with sponge layer was used.

To investigate the sensitivity to the treatment of the *outflow* BC we performed a number of simulations varying the velocity
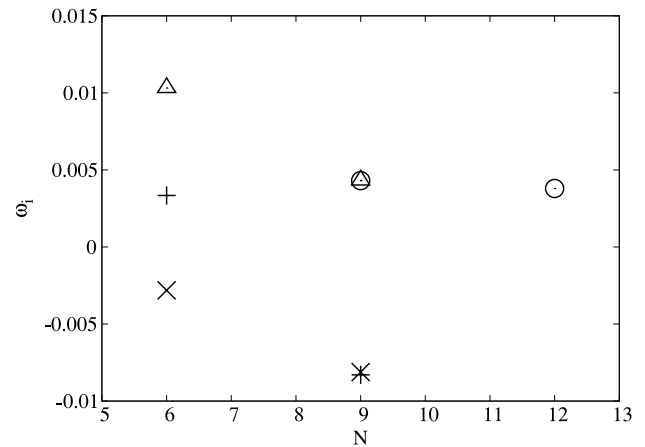
ratio R, box length L_x, mesh structure, polynomial order N and the noise level used to trigger the instability (selected setups are summarised in Table 1). For all studied cases there is an initial transient phase followed by a short phase of nearly exponential decay of time-dependent oscillations. Depending on the domain size and if additional noise was added or not, this phase ends with a rapid increase of disturbance amplitude followed by exponential decay/saturation, or with the slow growth of low-amplitude oscillations. A careful study of numerical convergence was necessary to determine the minimal domain length and sufficient resolution for the simulations. We found $N = 9$ and $L_x = 150$ to be adequate to achieve numerical convergence. Those runs show the critical velocity ratio R, at which the first bifurcation occurs, to lie in the range between 1.5 and 1.6.

3.2. Linear modal analysis

Here we present results of the linear global stability analysis, obtained using Nek5000 in an inflow–outflow setting. We start our discussion from the numerical convergence tests performed on meshes MS2 and MS3 ($L_x = 150$) with polynomial order $N = 6$ and 9 for $R = 1.5$, and on meshes MS3 ($L_x = 150$) and MS4 ($L_x = 250$) with $N = 6$, 9 and 12 for $R = 1.6$ respectively. Runs performed on mesh MS4 were used to confirm numerical convergence of our results with respect to box length and polynomial order.

Selected results of the convergence tests are shown in Fig. 4 presenting the growth rate of the strongest mode as a function of N and meshes. Symbols $+$ and $\times$ present results of the modal stability analysis for $R = 1.5$ and meshes MS2 and MS3, respectively. Symbols $\triangle$ and $\bigcirc$ show results of modal stability analysis for $R = 1.6$ and meshes MS3 and MS4. In all studied cases increasing resolution decreases the growth rates of all the modes (including the strongest one) until convergence is reached. The importance of high resolution is clearly evident. The dependency of the results on the domain length L_x was investigated with meshes MS3 and MS4 at $R = 1.6$ and $N = 9$. Both growth rates match each other proving $L_x = 150$ to be sufficient for numerical convergence. A final test was performed on mesh MS4 at $R = 1.6$ and $N = 12$, showing that the previously discussed results were really converged.

In Fig. 5 we present the converged spectra of the JCF for both $R = 1.5$ and 1.6 computed on mesh MS3 with $N = 9$. As the eigenvalues ω of the operator **A** come in complex pairs, the resulting spectra (growth rate ω_i versus frequency ω_r) are symmetric with respect to $\omega_r = 0$ and we utilise the negative and positive ω_r parts
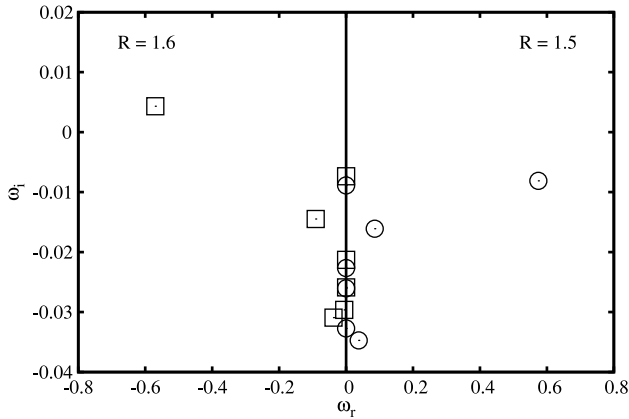
Fig. 5. The spectra of the JCF for MS3 mesh, $N = 9$ and different velocity ratios. As the spectra are symmetric with respect to $\omega_r = 0$ we utilise the negative and positive ω_r parts to compare different cases. The plot gives spectra for $R = 1.6$ (negative ω_r, $\square$) and $R = 1.5$ (positive ω_r, $\bigcirc$).
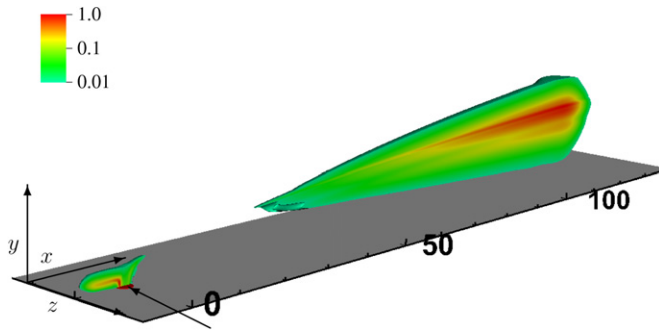

Fig. 6. Modulus of the strongest, complex eigenmode of the direct (far field) and adjoint (pipe orifice) operators. The plot presents volume visualisation of the modulus of the streamwise velocity component cut along the symmetry plane. Only values larger than 1% of the maximum modulus are shown. The pipe orifice is marked by an arrow and the sponge region starts at $x = 120$.

Fig. 7. Energy evolution for the transient growth of the optimal disturbance. Upper and lower plots correspond to the stable ($R = 1.5$) and unstable ($R = 1.6$) cases, respectively. Continuous and dashed curves (on both plots) represent the closed cycle with energy growth and decay in the direct and adjoint phases respectively.

to compare the two different cases. Comparison of both spectra confirms the critical velocity ratio to lie in the range between 1.5 and 1.6.

Fig. 6 shows the modulus of the streamwise velocity component of the strongest eigenmodes of the direct (far field) and adjoint (pipe vicinity) operators for $R = 1.5$ and $N = 9$. The pipe orifice is located at $x = 0$ and the modes' maxima are normalised to unity. The colour scale is logarithmic and all points with values smaller than 1% are made transparent. This illustrates strong spatial variation of the eigenmodes. The total growth of the direct mode (ratio of the maximum to the value at the pipe orifice) is of order 10^9. The visible strong streamwise separation of the direct and adjoint global modes is induced by the base-flow advection and is a signature of non-normality of the linearised operator. This is important since such a high degree of operator non-normality leads to great sensitivity of the corresponding eigenvalues [20]. It is also shown that, as a result of non-normality, the perturbation energy may experience strong transient growth even though the flow is globally stable.

4. Optimal perturbations

In this section we discuss results of linear optimal disturbances, which is a well established technique to identify the initial condition leading to the largest growth of the disturbance at finite time.

Our simulations were performed on the fine mesh MS3 ($L_x = 150$) with polynomial order $N = 9$, optimisation time $T = 77$ for
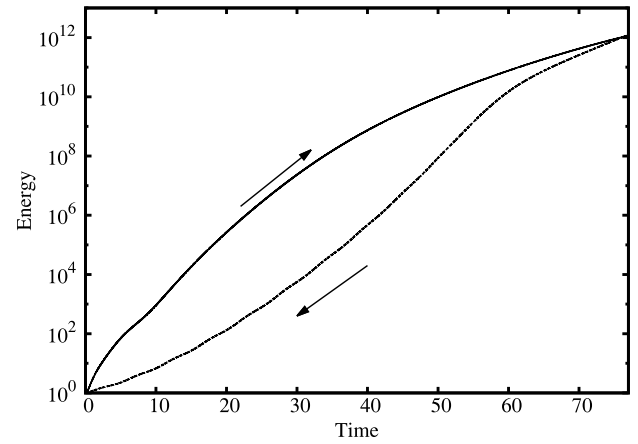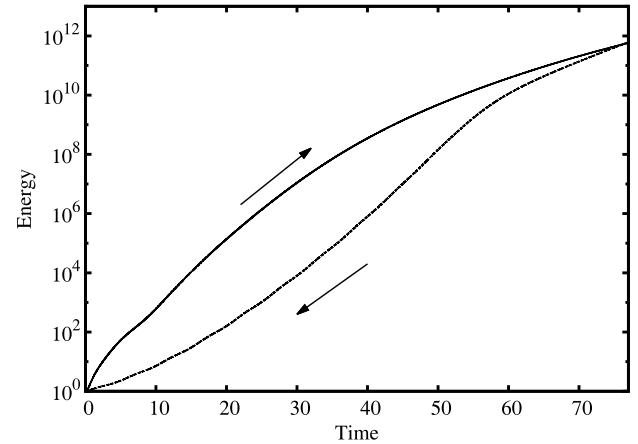
$R = 1.5$ and 1.6. The initial state $\vec{u}(0)$ for each of the step (direct and adjoint) was normalised $\langle \vec{u}(0), \vec{u}(0) \rangle = 1$, and the assumed convergence criterion was 5×10^{-5}, reached after 36 iterations. To keep the direct and adjoint problems consistent we apply sponge layers together with homogeneous Dirichlet BC both at the inflow and outflow in the flow. An important advantage of the non-modal analysis is its insensitivity to the outflow BC, as the travelling wave packet for adopted value of the optimisation time never reaches the outflow. The results are presented in Figs. 7–12.

Fig. 7 presents the energy growth with time for direct and adjoint phases for stable ($R = 1.5$; upper plot) and unstable ($R = 1.6$; lower plot) cases. The energy evolution is similar in both cases and its final value differs only by a factor of 2 ($E = 8 \times 10^{11}$ and 1.6×10^{12} for $R = 1.5$ and 1.6 respectively) showing the transient growth to be only weakly dependent on R. The calculated value of λ in Eq. (6) is 0.9972 and 0.9964 for R equal to 1.5 and 1.6, respectively.

Figs. 8 and 9 present a comparison of the optimal initial conditions for the streamwise velocity component $u_x(0)$ and corresponding final wave packet $u_x(T)$ for stable $R = 1.5$ and unstable $R = 1.6$ cases, respectively. Angled and top views are shown. As both the optimal initial conditions and wave packets are symmetric with respect to the grid symmetry plane ($y = 0$) we plot results of both simulations on a single frame placing the stable case in front/lower part of the plot. The maximum value of all the functions is normalised to unity, and the plotted isosurface corresponds to 0.2. The optimal initial condition resides at the foot of the CVP and consists of a number of the backward titling
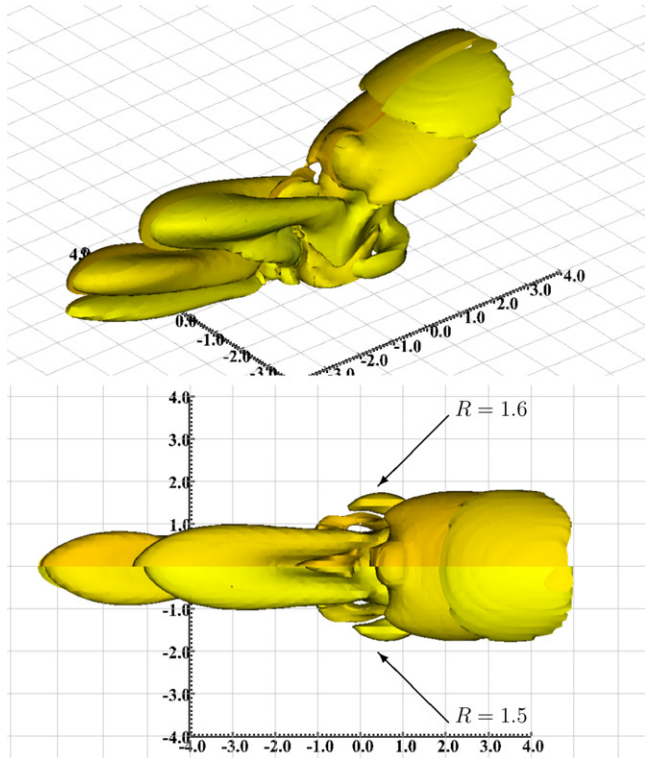
Fig. 8. Comparison of the optimal initial conditions for the stable (front, $R = 1.5$) and unstable (back, $R = 1.6$) cases. The maximum value of both functions is normalised to unity, and the plotted isosurface corresponds to 0.2. Angled and top views are presented.
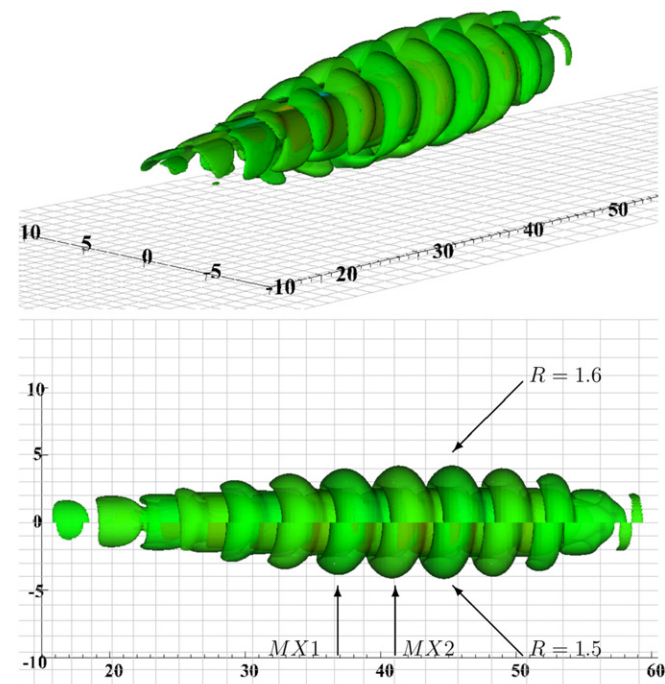

Fig. 9. Comparison of the resulting wave packet of the optimal disturbance for the stable (front, $R = 1.5$) and unstable (back, $R = 1.6$) cases. The maximum value of both functions is normalised to unity, and the plotted isosurface corresponds to 0.2. Angled and top views are presented. Two strongest local maxima are marked MX1 and MX2 (compare Fig. 10).

structures that develop into a growing wave packet propagating up the CVP. The structures visible in the wave packet correspond
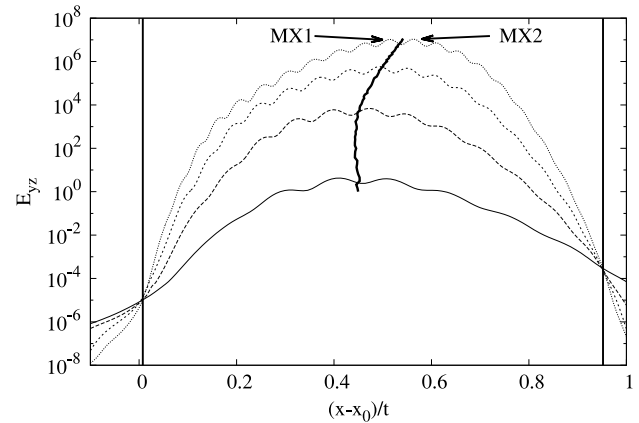

Fig. 10. Distribution of the cross-stream integrated energy E_{yz} of the wave packet as a function of the ray velocity $(x - x_0)/t$ for different times t. Thin continuous (lowest), long-dashed, short-dashed and dotted (highest) curves correspond to t equal to 18.75, 37.5, 56.25 and 75, respectively. The energy was re-scaled for consistency with Fig. 14. Vertical lines give the velocities of the leading (right) and trailing (left) edges of the wave packet. The continuous thick curve shows the position of the estimated maximum of the envelope of E_{yz}. Two strongest local maxima at time $t = 75$ are marked MX1 and MX2 (compare to Fig. 9). Data from linear simulation performed at $R = 1.5$.
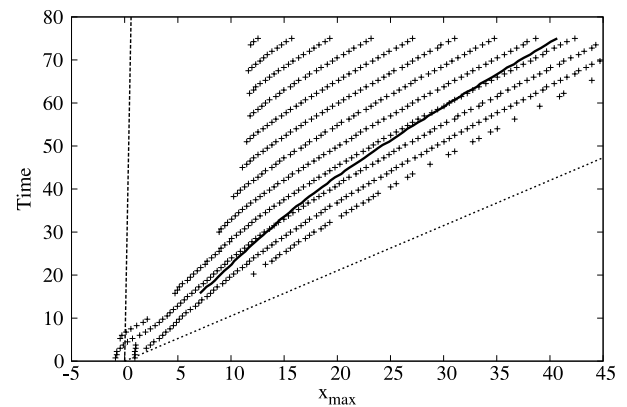

Fig. 11. Spatio-temporal diagram of the local maxima of E_{yz} (+). The positions of the leading and trailing edges of the wave packet are marked by the dotted and dashed lines, respectively. The continuous curve gives the position of the estimated envelope maximum. Linear simulation performed at $R = 1.5$.
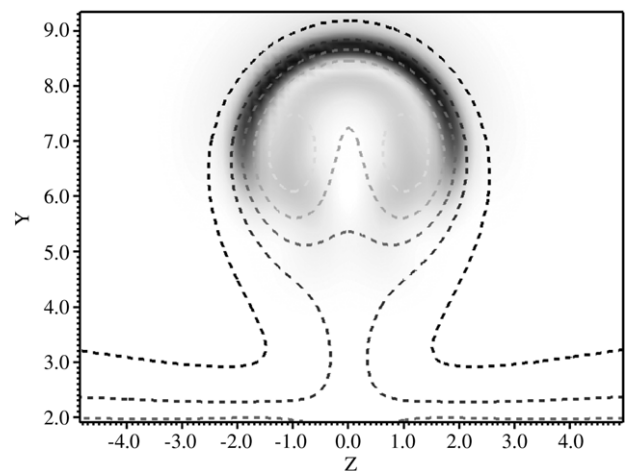

Fig. 12. Cross-stream cut through the base flow and the wave packet at streamwise position $x = 38.7$. The contour plot gives the distribution of the base flow streamwise velocity component, and the grey scale plot shows the energy of the perturbation at the wave packet maximum MX1 at time $t = 75$. Linear simulation performed at $R = 1.5$.
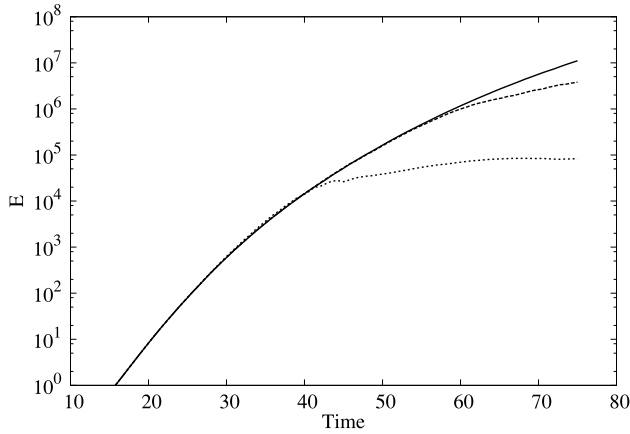
Fig. 13. Energy evolution for the transient growth of the optimal disturbance at $R = 1.5$ for the linear case (continuous curve) and the nonlinear DNS, in which the optimal disturbance was added on top of the steady base flow. Two nonlinear DNS cases are presented: $U_{OD} = 10^{-5}$ (dashed curve) and 10^{-4} (dotted curve). The interpolated streamwise maximum of E_{yz} is plotted as a function of time. For consistency with Figs. 10 and 14 the energy was re-scaled to 1.0 at time $t = 15.75$.

Fig. 14. Distribution of the cross-stream plane integrated energy E_{yz} as a function of the ray velocity $(x - x_0)/t$ for the nonlinear DNS performed at $R = 1.5$ and $U_{OD} = 10^{-4}$. For full description see Fig. 10.

to the local energy maxima presented in Figs. 10 and 11. The two strongest maxima located at $x = 38.7$ and 42.3 are marked MX1 and MX2. The alignment of the wave packet with the CVP in the base flow is clearly visible in Fig. 12 presenting the two-dimensional z–y cut at maximum MX1 through the base flow and the wave packet at $t = 75$. Both the optimal disturbances and wave packets for stable and unstable cases are almost identical. They are, however, slightly shifted with respect to each other due to different shape of the base flow. The wave packets differ also in their wavelength, which is slightly shorter for the stable case.

The evolution of the wave packet is also depicted in Figs. 10 and 11. Fig. 10 presents the spanwise fluctuation energy integrated over cross-stream plane y–z for a given streamwise position x. The integrated energy is plotted as a function of the ray velocity $(x - x_0)/t$, where x_0 is an initial position of the perturbation. Horizontal curves give the time evolution of E_{yz} starting from $t = 18.75$ (lowest curve) and ending at $t = 75$ (highest curve). The vertical lines give the propagation speed of the leading (right) and trailing (left) edges equal to $0.925U_\infty$ and $0.0075U_\infty$, respectively. The continuous thick, vertical curve in the middle shows the position of the estimated maximum of the E_{yz} envelope x_{max}. It is defined as the maximum of the parabola connecting the highest local energy maximum with its two neighbours. It should be noted here, that in the linear case the perturbation envelope could be computed by the Hilbert transform performed in the streamwise direction. However, this transform cannot be applied to the nonlinear DNS results (see Fig. 14), and for consistency we estimate the maximum position by parabolic interpolation in both cases. Fig. 11 gives the spatio-temporal diagram of the E_{yz} local maxima $(+)$, interpolated maximum position x_{max} (thick continuous curve) and the leading and trailing edges (dotted and dashed lines).

The amplitude growth of the oscillations between leading and trailing edges is clearly visible. At the same time, the wave packet is spreading in the streamwise direction and more and more local E_{yz} maxima emerge. The trailing edge velocity is small but positive, confirming the JCF at $R = 1.5$ to be convectively unstable. The plot of the interpolated streamwise maximum of the perturbation energy integrated over cross-stream planes as a function of time (continuous curve in Fig. 13) gives the growth rate of the most unstable waves travelling with a group velocity of about $0.5U_\infty$. It is interesting to note that the maximum is in fact slightly faster than the individual wave maxima travelling with a local phase velocity.
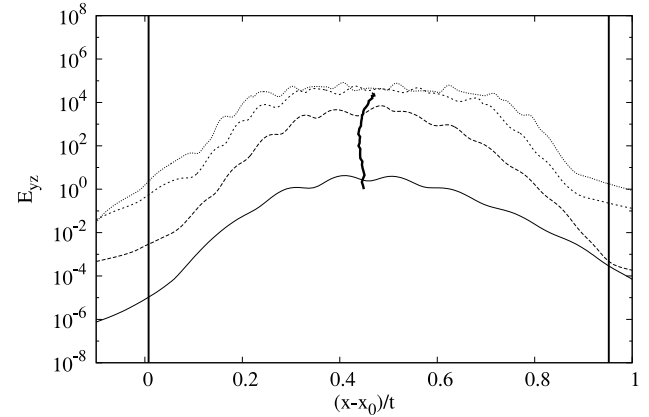
Fig. 12 presents the streamwise velocity contour plot for the nonlinear base flow, and the energy of the wave packet at the maximum MX1 (compare Figs. 9 and 10) in the cross-stream plane at the streamwise position $x = 38.7$. The wave packet is aligned with the shear layer surrounding the CVP and has a varicose symmetry when viewed from top (x–z plane). This suggests the instability to be of inviscid inflectional type triggered by the regions of high vertical shear on top of the CVP.

In addition we performed the nonlinear DNS, in which the rescaled optimal disturbance added on top of the steady base flow is used as initial condition. The control parameter is here the initial maximum value of the optimal disturbance velocity U_{OD} rescaled in our simulations to 10^{-5} and 10^{-4}. The simulations were performed on mesh MS3 for $N = 9$ and the velocity ratio R equal 1.5 and 1.6. The velocity perturbation in nonlinear DNS is defined as the difference between the actual value of the velocity and the steady base flow at the same location. The comparison of the perturbation energy growth at $R = 1.5$ for the linear simulation and two DNS with $U_{OD} = 10^{-5}$ and 10^{-4} is presented in Fig. 13. To match different curves the computed energy is re-scaled to 1.0 at time $t = 15.75$. The initial energy evolution is identical for all the simulations, however, the nonlinear DNS finally saturate at around $4 \cdot 10^{-3}$ (non-rescaled value). Fig. 14 presents the spanwise fluctuation of the perturbation energy integrated over cross-stream plane y–z for a given streamwise position x. The phases of the initial linear evolution followed by the nonlinear one are clearly visible (saturation for larger times, compare to Fig. 10). Another manifestation of nonlinearity is an apparent destabilisation of the velocity field at ray velocities lower than the trailing edge and higher than the leading edge velocities of the linear wavepacket, respectively. This corrugation of the wavepacket edges, seen as an apparent energy increase in Fig. 14 for low and high velocities, is a transient phenomenon ending at time about $t = 120$ and it is difficult to interpret this as nonlinear absolute instability discussed by Chomaz [43]. Note that for the zero velocity ray $x = x_0$ the nonlinear transient energy increase is followed by exponential decay; yielding nonlinear absolute stability.

The evolution of the time-dependent amplitude of a single Fourier component in the signal of the velocity probe (located 15 units downstream from the jet centre) for the DNS with $U_{OD} = 10^{-5}$ is presented in Fig. 15 (continuous and dashed curves correspond to $R = 1.5$ and 1.6, respectively). The chosen (temporal) Fourier component is the most dominant one in the flow, and its amplitude at time t is calculated by projection of the signal on sine and cosine functions within the window $(t - T_p/2, t + T_p/2)$ (T_p being the component period). The initial amplitude development
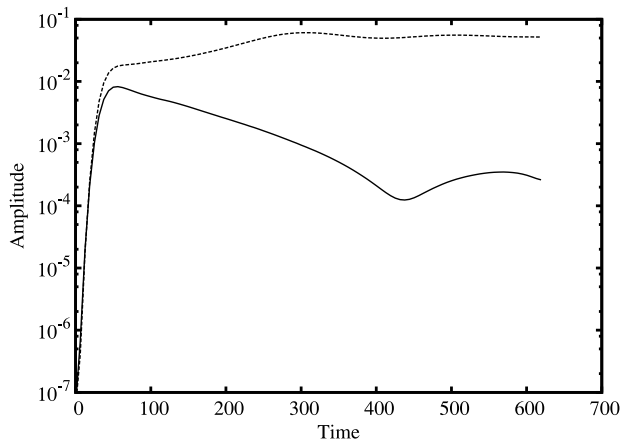
Fig. 15. Temporal evolution of the disturbance amplitude for the transient growth of the optimal disturbance in the nonlinear DNS. Continuous and dashed curves correspond to the stable ($R = 1.5$) and unstable ($R = 1.6$) cases, respectively.
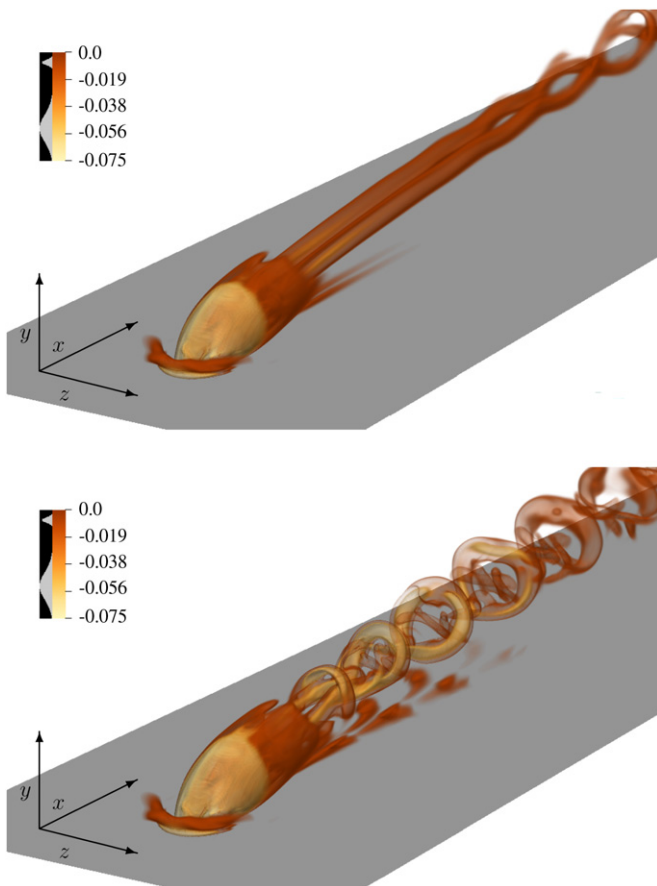

Fig. 16. Comparison of the asymptotic fate for the optimal disturbance added on top of the base flow in the nonlinear DNS. Upper and lower plots correspond to the stable ($R = 1.5$) and unstable ($R = 1.6$) cases, respectively. The plots show the vortical structure of the flow at time $t = 630$ after the disturbance was added using volume rendering of the λ_2 vortex identification criterion.

is identical both for stable and unstable cases, however the final (asymptotic) fate is consistent with modal analysis.

Snapshots from the nonlinear simulations showing the vortical structure of the flow at time $t = 630$ can be seen in Fig. 16. The optimal disturbance was added to the base flow and various features of the flow are visualised using volume rendering of the λ_2 vortex identification criterion [39]. The colour map and the transfer function for the volume rendering are chosen so that the regions of

highly negative values of λ_2 are coloured in yellow (vortex 'cores'), and the regions of lower magnitude, i.e., negative value closer to zero, are coloured in brown (vortex 'edges'). In the stable case $R = 1.5$ the CVP are clearly visible and almost time independent. For the unstable case $R = 1.6$ we can see the limit cycle with the CVP broken down into a series of hairpin vortices characteristic of a shear layer instability. They are similar to the hairpin vortices observed by Ilak et al. (see e.g. Fig. 2 in Ref. [15]).

5. Discussion and conclusions

In the current work we performed a stability analysis of the jet in crossflow (JCF) testing two numerical methods applied for stability computations. We focused on the calculation of the critical velocity ratio R at which the first bifurcation (transition from the steady to unsteady flow) occurs. We performed a number of simulations using different numerical methods and codes, namely a fully spectral (Fourier–Chebyshev) and spectral element discretisation (SEM). We find the JCF to be so sensitive to the simulation parameters and setup that the critical velocity ratio is easily influenced by the numerical setup. In particular we found that methods based on streamwise Fourier decomposition to be not well suited for the present case which is dominated by considerable disturbance growth through the domain. The periodic boundary conditions (BCs) in the streamwise direction together with a fringe region may provide insufficient damping and can thus significantly change the flow dynamics. Even for codes with inflow/outflow BC we demonstrate the sensitivity of the modal stability analysis to the grid resolution, the location of the outflow and thus to the length of the computational domain.

This great sensitivity of the eigenvalue at the bifurcation point is a manifestation of strong non-normality of the evolution operator, which is characteristic to open flows and is mainly related to downstream base flow advection $\vec{U}_b \cdot \nabla \vec{u}$ in the linearised operator. The degree of the operator non-normality can be measured by the scalar product between the adjoint and direct global modes and can be seen as streamwise separation between the adjoint and direct modes (Fig. 6). The strong non-normality leads to abrupt bifurcation and makes the global eigenvalue spectrum not a robust quantity, as small perturbations (e.g. external forcing, noise, round-off and other discretisation errors) can destabilise or stabilise the flow. That is why the first bifurcation point for the JCF is difficult to determine both numerically and experimentally. Our highest resolution runs performed in the longest ($L_x = 250$) computational domain show the critical velocity ratio to lie within the range $R \in (1.5, 1.6)$. We have to stress that this computational domain is about 10 times larger than the dynamically significant region, as the overlap of the strongest direct and adjoint global modes (the wavemaker) is located within 25 units from the jet orifice. Note that the cited value for the bifurcation relates to the jet modelled as a steady inhomogeneous Dirichlet condition on the plate surface.

Concepts developed for linear non-normal operators can be also used to describe other types of behaviour of open flows like transient growth. We computed the optimal disturbance using the direct and the adjoint operator and find its growth (of the order 10^{12} within the domain) and shape robust and almost identical for both stable ($R = 1.5$) and unstable ($R = 1.6$) cases. It is consistent with the linear theory of non-normal operators, where, in the case of strong non-normality close to the global instability threshold, the energy of the perturbation can undergo large transient growth inversely proportional to the scalar product between the adjoint and direct global modes. This non-modal analysis confirmed our previous results, showing the JCF at $R = 1.5$ to be convectively unstable. On the other hand the small value of the trailing edge velocity $0.0075U_\infty$ suggests the critical value of the velocity ratio

R to be close to 1.5. We also found the instability to be of inviscid inflectional type triggered by the regions of high vertical shear on top of the counter-rotating vortex pair (CVP).

Prediction of both modal and non-modal linear analyses is consistent with our converged nonlinear DNS simulations, where the perturbation undergoes first large transient growth which is followed by exponential growth or decay related to the asymptotic fate related to the growth rate associated with a particular global mode. The modes give good qualitative description of the flow dynamics showing both the harmonic amplifier behaviour and the associated transient growth of initial perturbations to be related to the special non-normality of the linear evolution operator associated with open flows.

Acknowledgements

References

[1] T.F. Fric, A. Roshko, Vortical structure in the wake of a transverse jet, J. Fluid Mech. 279 (1994) 1–47. http://dx.doi.org/10.1017/S0022112094003800.
[2] R.M. Kelso, T.T. Lim, A.E. Perry, An experimental study of round jets in cross-flow, J. Fluid Mech. 306 (1996) 111–144. http://dx.doi.org/10.1017/S0022112096001255.
[3] S.H. Smith, M.G. Mungal, Mixing, structure and scaling of the jet in crossflow, J. Fluid Mech. 357 (1998) 83–122.
[4] T.T. Lim, T.H. New, S.C. Luo, On the development of large-scale structures of a jet normal to a cross flow, Phys. Fluids 13 (2001) 770–775. http://dx.doi.org/10.1063/1.1347960.
[5] S. Megerian, J. Davitian, L.S. de B. Alves, A.R. Karagozian, Transverse-jet shear-layer instabilities. Part 1. Experimental studies, J. Fluid Mech. 593 (2007) 93–129. http://dx.doi.org/10.1017/S0022112007008385.
[6] J. Davitian, D. Getsinger, C. Hendrickson, A.R. Karagozian, Transition to global instability in transverse-jet shear layers, J. Fluid Mech. 661 (2010) 294–315. http://dx.doi.org/10.1017/S0022112010003046.
[7] S.L.V. Coelho, J.C.R. Hunt, The dynamics of the near field of strong jets in crossflows, J. Fluid Mech. 200 (1989) 95–120.
[8] L. Cortelezzi, A.R. Karagozian, On the formation of the counter-rotating vortex pair in transverse jets, J. Fluid Mech. 446 (2001) 347–373. http://dx.doi.org/10.1017/S0022112001005894.
[9] L.L. Yuan, R.L. Street, J.H. Ferziger, Large-eddy simulations of a round jet in crossflow, J. Fluid Mech. 379 (1999) 71–104.
[10] S. Muppidi, K. Mahesh, Study of trajectories of jets in crossflow using direct numerical simulations, J. Fluid Mech. 530 (2005) 81–100. http://dx.doi.org/10.1017/S0022112005003514.
[11] S. Muppidi, K. Mahesh, Direct numerical simulation of round turbulent jets in crossflow, J. Fluid Mech. 574 (2007) 59–84. http://dx.doi.org/10.1017/S0022112006004034.
[12] J. Ziefle, L. Kleiser, Large-Eddy simulation of a round jet in crossflow, AIAA J. 47 (2009) 1158–1172. http://dx.doi.org/10.2514/1.38465.
[13] S. Bagheri, P. Schlatter, P.J. Schmid, D.S. Henningson, Global stability of a jet in crossflow, J. Fluid Mech. 624 (2009) 33. http://dx.doi.org/10.1017/S0022112009006053.
[14] P. Schlatter, S. Bagheri, D.S. Henningson, Self-sustained global oscillations in a jet in crossflow, Theor. Comput. Fluid Dynam. 25 (2011) 129–146. http://dx.doi.org/10.1007/s00162-010-0199-1.
[15] M. Ilak, P. Schlatter, S. Bagheri, D.S. Henningson, Bifurcation and stability analysis of a jet in cross-flow: onset of global instability at a low velocity ratio, J. Fluid Mech. 696 (2012) 94–121. http://dx.doi.org/10.1017/jfm.2012.10.
[16] A.R. Karagozian, Transverse jets and their control, Prog. Energy Combust. Sci. 36 (2010) 531–553. http://dx.doi.org/10.1016/j.pecs.2010.01.001.
[17] K. Mahesh, The interaction of jets with crossflow, Annu. Rev. Fluid Mech. 45 (2013) 379–407. http://dx.doi.org/10.1146/annurev-fluid-120710-101115.
[18] R.M. Kelso, A.J. Smits, Horseshoe vortex systems resulting from the interaction between a laminar boundary layer and a transverse jet, Phys. Fluids 7 (1995) 153–158. http://dx.doi.org/10.1063/1.868736.
[19] P. Huerre, P.A. Monkewitz, Local and global instabilities in spatially developing flows, Annu. Rev. Fluid Mech. 22 (1990) 473–537. http://dx.doi.org/10.1146/annurev.fl.22.010190.002353.
[20] J.M. Chomaz, Global instabilities in spatially developing flows: non-normality and nonlinearity, Annu. Rev. Fluid Mech. 37 (2005) 357–392. http://dx.doi.org/10.1146/annurev.fluid.37.061903.175810.
[21] V. Theofilis, Global linear instability, Annu. Rev. Fluid Mech. 43 (2011) 319–352. http://dx.doi.org/10.1146/annurev-fluid-122109-160705.
[22] S. Reddy, P. Schmid, D. Henningson, Pseudospectra of the Orr-Sommerfeld equation, SIAM J. Appl. Math. 53 (1993) 15–47. http://dx.doi.org/10.1137/0153002.
[23] B. Galletti, A. Bottaro, Large-scale secondary structures in duct flow, J. Fluid Mech. 512 (2004) 85–94. http://dx.doi.org/10.1017/S0022112004009966.
[24] D. Obrist, P.J. Schmid, On the linear stability of swept attachment-line boundary layer flow. Part 2. Non-modal effects and receptivity, J. Fluid Mech. 493 (2003) 31–58. http://dx.doi.org/10.1017/S0022112003005780.
[25] U. Ehrenstein, F. Gallaire, Two-dimensional global low-frequency oscillations in a separating boundary-layer flow, J. Fluid Mech. 614 (2008) 315. http://dx.doi.org/10.1017/S0022112008003285.
[26] H.M. Blackburn, D. Barkley, S.J. Sherwin, Convective instability and transient growth in flow over a backward-facing step, J. Fluid Mech. 603 (2008) 271–304. http://dx.doi.org/10.1017/S0022112008001119.
[27] O. Marquet, D. Sipp, J.-M. Chomaz, L. Jacquin, Amplifier and resonator dynamics of a low-Reynolds-number recirculation bubble in a global framework, J. Fluid Mech. 605 (2008) 429–443. http://dx.doi.org/10.1017/S0022112008000323.
[28] E. Åkervik, J. Hœpffner, U. Ehrenstein, D.S. Henningson, Optimal growth, model reduction and control in a separated boundary-layer flow using global eigenmodes, J. Fluid Mech. 579 (2007) 305–314. http://dx.doi.org/10.1017/S0022112007005496.
[29] A.S. Sharma, N. Abdessemed, S.J. Sherwin, V. Theofilis, Transient growth mechanisms of low Reynolds number flow over a low-pressure turbine blade, Theor. Comput. Fluid Dynam. 25 (2011) 19–30. arXiv:1302.2770 http://dx.doi.org/10.1007/s00162-010-0183-9.
[30] U. Ehrenstein, F. Gallaire, On two-dimensional temporal modes in spatially evolving open flows: the flat-plate boundary layer, J. Fluid Mech. 536 (2005) 209–218. http://dx.doi.org/10.1017/S0022112005005112.
[31] P. Schmid, D.S. Henningson, Stability and Transition in Shear Flows, Springer, 2001.
[32] M. Chevalier, P. Schlatter, A. Lundbladh, D.S. Henningson, SIMSON: A Pseudo-Spectral Solver for Incompressible Boundary Layer Flows, in: Tech. Rep., KTH, Sweden, 2007.
[33] P.F. Fischer, J.W. Lottes, S.G. Kerkemeier, 2008, nek5000 Web page, http://nek5000.mcs.anl.gov..
[34] J. Nordström, N. Nordin, D. Henningson, The fringe region technique and the fourier method used in the direct numerical simulation of spatially evolving viscous flows, SIAM J. Sci. Comput. 20 (1999) 1365–1393.
[35] D.S. Henningson, E. Åkervik, The use of global modes to understand transition and perform flow control, Phys. Fluids 20 (3) (2008) 031302.
[36] A. Peplinski, P. Schlatter, D.S. Henningson, Stability tools for the spectral-element code nek5000: Application to jet-in-crossflow, in: M. Azaiez, H. El Fekih, J. Hesthav (Eds.), Spectral and High Order Methods for Partial Differential Equations—ICOSAHOM 2012, Springer International Publishing, 2014, pp. 349–359.
[37] S. Bagheri, E. Åkervik, L. Brandt, D.S. Henningson, Matrix-free methods for the stability and control of boundary layers, AIAA J. 47 (2009) 1057–1068. http://dx.doi.org/10.2514/1.41365.
[38] R. Lehoucq, D. Sorensen, C. Yang, ARPACK Users Guide: Solution of Large Scale Eigenvalue Problems by Implicitly Restarted Arnoldi Methods, 1997.
[39] J. Jeong, F. Hussain, On the identification of a vortex, J. Fluid Mech. 285 (1995) 69–94. http://dx.doi.org/10.1017/S0022112095000462.
[40] E. Åkervik, L. Brandt, D.S. Henningson, J. Hœpffner, O. Marxen, P. Schlatter, Steady solutions of the Navier–Stokes equations by selective frequency damping, Phys. Fluids 18 (068102) (2006) 1–4. http://dx.doi.org/10.1063/1.2211705.
[41] A. Monokrousos, E. Åkervik, L. Brandt, D.S. Henningson, Global three-dimensional optimal disturbances in the Blasius boundary-layer flow using time-steppers, J. Fluid Mech. 650 (2010) 181–214. http://dx.doi.org/10.1017/S0022112009993703.
[42] S. Rolshoven, A Mechanism of Transition to Turbulence in a Three-Dimensional Boundary Layer, in: Tech. Rep., LadHyX, École Polytechnique, France, 2000.
[43] J.M. Chomaz, Absolute and convective instabilities in nonlinear systems, Phys. Rev. Lett. 69 (1992) 1931–1934. http://dx.doi.org/10.1103/PhysRevLett.69.1931.